Laser-Driven Magnetic Flux Compression for Magneto-Inertial Fusion

Introduction

Direct-drive inertial confinement fusion (ICF) has seen formidable progress in recent years.[1,2] The energy coupling and hydrodynamics of the implosion continue to be the dominant factors in the path to successful conversion of the incident laser energy E_L into thermonuclear burn energy E_{TN} (Ref. 3). For direct-drive implosions, the energy gain $G = E_{\mathrm{TN}}/E_L$ depends strongly on the implosion velocity V_i and on the coupling efficiency $\eta_c = \eta_{\mathrm{abs}}\eta_h$. The dominant part of this product is the hydrodynamic efficiency η_h, the ratio of the kinetic energy of the implosion to the incident laser energy E_L (a few percent), while the absorption efficiency η_{abs} is of the order of 60% to 80% depending on the laser wavelength. It can be shown[4] that the gain of an ignited target scales as $G \sim \eta_h V_i^{-2}$, while η_h is approximated well with $\eta_h \sim V_i^{-0.75} I_L^{-0.25}$, where I_L is the laser intensity. Thus, the thermonuclear gain is roughly inversely proportional to the implosion velocity. On the other hand, successful ignition of the assembled central hot spot (the necessary condition for any gain in ICF) in conventional ICF requires that the hot spot reaches a certain temperature T_{hs} (of the order of 5-keV ion temperature), which requires high implosion velocities. This is confirmed by the scaling relations of Ref. 4, which show that $T_{\mathrm{hs}} \sim V_i^{1.4}$. Too slow a compression will not compensate thermal losses and the hot spot will not reach the required temperature, although the areal density of the fuel may attain high values. These restrictions on V_i set limits on both the minimum energy for ignition and the maximum gain in conventional ICF.

In what is called a magneto-inertial fusion (MIF) implosion, an additional thermal insulation of the fuel forming the hot spot is provided by a strong magnetic field in a typical direct-drive ICF target.[5] The hot spot can reach ignition temperatures due to the reduced electron thermal conductivity, and then, when the nuclear burn develops, the alpha particles will also be confined to the burn region, delivering the energy needed to support the burn wave. Considering a hot spot with a characteristic radius $R_h = 40\ \mu$m, a density of ~10 g/cc, and a temperature of 5 keV, an electron–cyclotron frequency ω_{ce} exceeding the collision frequency ν_e is required for magnetic insulation; i.e., $\omega_{\mathrm{ce}}\tau_e > 1$, where $\tau_e = 1/\nu_e$ is the collision time. This corresponds to $B > 10$ MG due to the high densities (small collision times) in the hot spot. The condition for alpha-particle confinement $r_\alpha/R_h < 1$ (where r_α is the gyroradius) requires $B > 95$ MG for the 3.5-MeV fusion alphas in a burning DT plasma. Such strong magnetic fields are very difficult to create externally. The largest macroscopic magnetic fields have so far been generated only by magnetic-flux compression in metallic liners driven by chemical detonation.[6,7] The measured upper limit that we are aware of is of the order of 10 MG (Ref. 8). Flux compression with an ICF-scale laser like OMEGA[9] is a possible way to obtain even stronger fields. The idea is to perform an ICF implosion in which there is a preimposed macroscopic magnetic field, amplified with the compression of the target plasma. Flux compression with a plasma "liner" was discussed by Liberman and Velikovich in Refs. 10 and 11 more than 20 years ago. In Ref. 11 the authors consider a magnetic field that is "frozen" in plasma compressed by a thin cylindrical wall. They show effective compression of the field with low field diffusion losses. *Z* pinches and laser ablation are mentioned as possible drivers for the hydrodynamic compression of the plasma.

The basic concept of flux compression can be described with the following simple formulas. In cylindrical geometry, neglecting the diffusion of the magnetic field, the conservation of the magnetic flux Φ will yield an increase proportional to the reduction of the encircled area:

$$B_{\max} = B_0\left(\frac{r_0}{r_{\min}}\right)^2 \frac{\Phi}{\Phi_0} = B_0\left(\frac{r_0}{r_{\min}}\right)^2. \tag{1}$$

In the general case of nonzero flux diffusion out of the confining volume, the flux compression equation is obtained from Eq. (1) by differentiation:

$$\frac{1}{B}\frac{\mathrm{d}B}{\mathrm{d}t} = \frac{1}{\Phi}\frac{\mathrm{d}\Phi}{\mathrm{d}t} - \frac{2}{r(t)}\frac{\mathrm{d}r(t)}{\mathrm{d}t}. \tag{2}$$

This can be expressed in terms of the implosion velocity $V_i = -\mathrm{d}r(t)/\mathrm{d}t$ and the speed of resistive field diffusion $V_f = \eta/\mu_0\delta$,

where η is the plasma resistivity, μ_0 is the permeability of vacuum, and δ is a characteristic scale length of the conductor (plasma) shell in question. The ratio $\mathrm{Re}_m V_i / V_f$ is the magnetic Reynolds number, the dimensionless metric that determines the effectiveness of the flux compression scheme. It is the ratio of the convective to the dissipative term in the magnetic flux equation and as such determines the magnetohydrodynamic (MHD) regime (from ideal MHD at $\mathrm{Re}_m \gg 1$ to strictly resistive MHD at $\mathrm{Re}_m < 1$). The speed V_f can be obtained from the time scale[12] of an assumed exponential flux decay through the conductive region interface (with scale length δ), given by the ratio of shell inductance $\mu_0 \pi r^2$ to resistance $\delta/(2\pi r\eta)$ (per unit axial length):

$$\tau = -\left(\frac{\mathrm{d}\ln\Phi}{\mathrm{d}t}\right)^{-1} = \frac{\mu_0 r\delta}{2\eta} = \frac{r}{2V_f}.$$

Expressing (2) in terms of Re_m yields

$$\frac{1}{B}\frac{\mathrm{d}B}{\mathrm{d}t} = -\frac{2V_f}{r(t)} + \frac{2V_i}{r(t)} = -\frac{1}{r(t)}\frac{\mathrm{d}r}{\mathrm{d}t}\left(1 - \frac{1}{\mathrm{Re}_m}\right) \tag{3}$$

and shows that the field will increase only if V_i is much larger than V_f, i.e., $\mathrm{Re}_m \gg 1$. Thus, when the diffusion of flux into the plasma shell due to its finite resistivity is considered, Eq. (1) is modified to

$$B_{\max} = B_0\left(\frac{r_0}{r_{\min}}\right)^{2\left(1-\frac{1}{\langle \mathrm{Re}_m\rangle}\right)}, \tag{4}$$

which follows from Eq. (3) for the simple case of Re_m constant in time (or equal to an appropriately chosen average value $\langle \mathrm{Re}_m \rangle$).

The OMEGA laser[9] is an ideal test bed for magnetic-flux-compression experiments in plasmas [Fig. 110.1(a)]. Typical implosion velocities V_i in excess of 10^7 cm/s, coupled with the high conductivity of the hot plasma containing the field, should keep the magnetic Reynolds number large and provide for effective compression of the seed magnetic flux. The seeding of a magnetic field in the target can be accomplished with a coil system driven by a device such as the one shown in Fig. 110.1(b) and described later in this text. In contrast to compression with metallic liners, an ICF-scale, cylindrical-ablator shell (usually plastic) driven by a laser does not by itself trap the enclosed magnetic flux, but delivers kinetic energy to the plasma that contains the field. This is the gas fill that is ionized by the initial hydrodynamic shock to a highly conductive plasma state in which the resident seed magnetic field is captured. At the onset of the laser pulse, the rapid increase in ablation pressure drives this shock through the shell; it breaks out into the gas, filling the capsule, and fully ionizes it, raising the temperature in the gas post-shock region to about 100 eV. It is this region with a high magnetic Reynolds number (a time-averaged value of $\mathrm{Re}_m > 60$ is obtained from the simulations) that traps the magnetic field. The colder and more-resistive shell then provides the mechanical work for compression of this plasma and the field embedded in it. Figure 110.2 shows the simulated electron-temperature

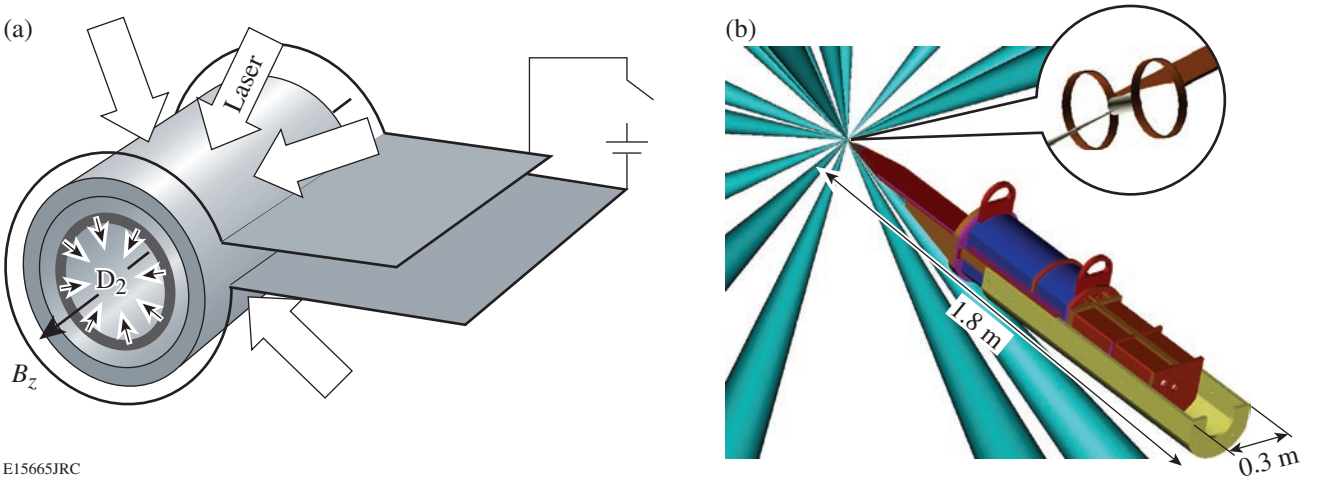

Figure 110.1
(a) Target-coil geometry for magnetic-flux-compression experiments. The cylindrical target is compressed radially by the laser beams. A single-turn coil delivers the seed magnetic pulse. (b) A compact, capacitive discharge system designed for integration in multibeam OMEGA experiments drives the current in the coils.

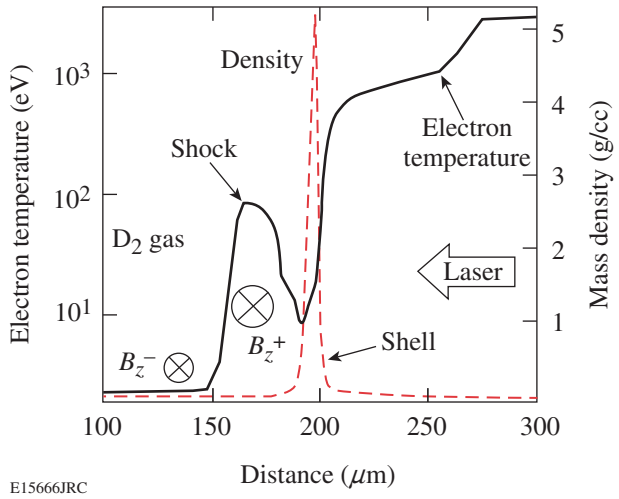

Figure 110.2
The imploding shell (peak in dashed curve) compresses the shock-ionized gas fill that has trapped the axial magnetic field in the hot post-shock region.

profile in the D_2 gas fill during shock propagation. This is for a 1.5-mm-long, 860-μm-diam, 20-μm-thick cylindrical plastic shell filled with 3 atm of D_2. The plastic shell can be identified in the density profile plotted at the same time. It is interesting to note that there is diffusion of magnetic flux out of the post-shock region not only through the shell but also into the unshocked gas inside the target (Fig. 110.2). This is driven by the steep gradient in resistivity and the short scale length of the shock interface, leading to a very large value of the diffusion speed. The simulation confirms it with an increase in the magnetic field ahead of the shock. The shock-front diffusion speed is

$$V_f = \frac{\eta^-}{\mu_0}\frac{1}{B_z^-}\frac{\partial B_z^-}{\partial r}, \tag{5}$$

where the "–" denotes the pre-shock region. For our case, if we consider the good approximation $\eta^- \gg \eta^+ \to 0$, an integration of the induction equation across the shock will yield a jump condition written in the frame of reference of the shock front moving with velocity u_s,

$$u_s B_z^- - \frac{\eta^-}{\mu_0}\frac{\partial B_z^-}{\partial r} = (u_s - V_i)B_z^+ . \tag{6}$$

This can be rewritten as

$$\frac{B_z^+}{B_z^-} = \frac{u_s - V_f}{u_s - V_i} . \tag{7}$$

This ratio shows that field cumulation in the post-shock region (large field ratio) needs large V_i, while V_f acts to reduce the field jump by raising the field ahead of the shock. In contrast, at the ionized gas–shell interface, the resistivity scale length is larger and the shell plasma is a conductor, albeit not as good as the plasma in the post-shock region. This leads to lower outward diffusion of the field and net flux compression due to the high convergence velocity of the shell. The field and density profiles at the center of the target, as simulated by *LILAC*-MHD,[13] are shown in Fig. 110.3 for the time of peak compression. One can see that in the hot spot (in this case the central 20 μm of the target) the magnetic field reaches the values (>95 MG) needed for alpha-particle confinement in a DT fusion target. The result is a six-fold increase in the simulated stagnation ion temperature to >7 keV, when compared to a simulation with no seed field.

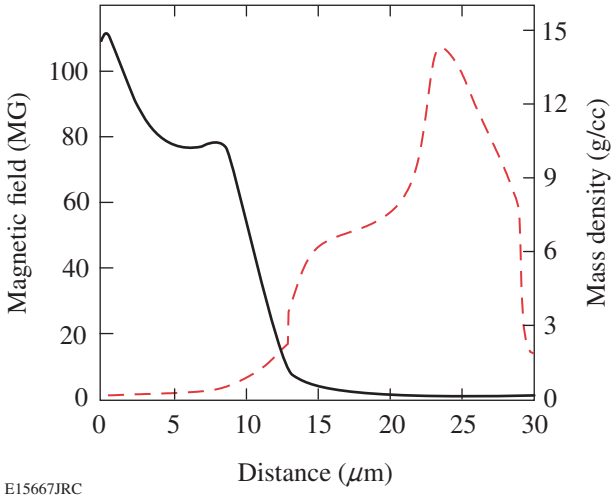

Figure 110.3
LILAC-MHD results for a 3-atm, D_2-filled CH capsule at the time of peak compression: field (solid curve) and density (dashed curve) profiles at the target center.

MIFEDS (Magneto-Inertial Fusion Energy Delivery System) Seed-Field Generator

To obtain multi-megagauss fields with the laser-driven flux-compression (LDFC) scheme, it is necessary to start from substantial seed-field values due to the limit in maximum convergence ratio of the compression. For a cylindrical geometry [Fig. 110.1(a)], the convergence ratio is between 10 and 20. Supplying tens of tesla to the target chamber center of OMEGA is nontrivial since the parametric space is restricted on one side by the small physical volume available and on the other by the need of high energy in the magnetic pulse. This is actually a high-power requirement because of the short duration of an

OMEGA implosion (1-ns pulses are used in the experiments). A compact device shown in Fig. 110.4 [see also Fig. 110.1(b)] generating seed magnetic fields of sufficient strength (up to 0.15 MG measured) was built to test the laser-driven magnetic-flux-compression concept. It fits in a diagnostic insertion port on the OMEGA chamber, stores not more than 150 J, and provides magnetic pulses with an intensity of 0.1 to 0.15 MG and ~400-ns duration.

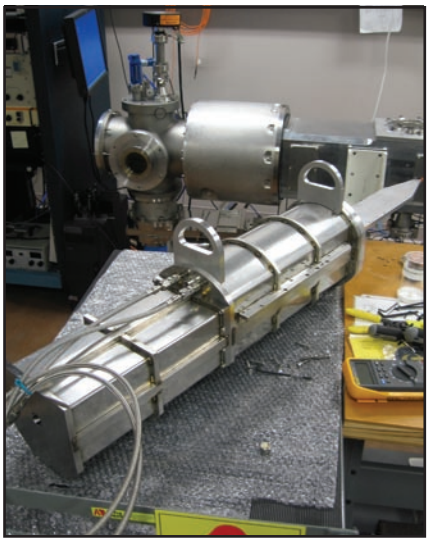

E15668JRC

Figure 110.4
MIFEDS device in the diagnostic TIM (ten-inch manipulator) facility.

The interaction volume in the OMEGA target chamber is characterized by the target size and is thus limited to a linear dimension of a few millimeters. This small volume is in the field of view of an extensive suite of diagnostics, pointed at the target chamber center from various angles and occupying conical space envelopes that should not be broken to prevent beam clipping or conflict/collision with other diagnostics. For the LDFC scheme described above, a magnetic pulse of sufficient strength must be delivered to the target interaction volume within such an envelope, and the field must be created by coils that do not obscure laser beams aimed at the target nor the view of the various diagnostics. Such restrictions point at low-mass, single-turn coils as the best solution. For a cylindrical target configuration, a Helmholtz-type coil provides advantageous geometry since a large number of laser beams can be pointed at the target in between the two coils without obscuration. An optimization of the field-to-coil current ratio

$$B_z/I \approx \mu_0 R^2\left(R^2 + D^2/4\right)^{-3/2}, \tag{8}$$

with the incident laser beams taken into account, leads to a choice of radius R for each and separation D between the coils that deviates from the standard Helmholtz coil where $R = D$. In the design suitable for OMEGA experiments, $R = 2.0$ mm and $D = 4.4$ mm. Figure 110.1(b) shows a cylindrical target with a typical diameter of 860 μm as it is placed between coils with the above dimensions. The coils were made from copper-clad Kapton foil with a thickness of 100 μm and an individual coil width of 0.5 mm. The inductance of such a single-turn coil is very low. The calculated value, obtained from both an analytical formula and simulations of the coil's magnetic energy with the magnetostatic code Radia,[14] was ~25 nH, consistent with measurements. To receive most of the energy stored in the charging circuit, the coil inductance must be the dominant portion of the total circuit inductance. If this is observed, the resulting low-inductance circuit will provide the stored energy in a very fast discharge pulse. Since our reference time scale—the duration of the laser-driven implosion—is less than 3 ns, this fast discharge is warranted, reducing the total energy required for the generation and support of the seed magnetic field. A discharge pulse that lasts hundreds of nanoseconds will provide a large time window at peak current/field. A very fast discharge is, in fact, required with this type of low-mass (9-mg total measured mass of the two turns in the base design) coil since the peak current values must be reached before the joule heating destroys the coil and quenches the current rise. The rate of temperature rise, determined from the specific heating rate $j^2\eta$, where j is the current density and η is the resistivity, can be written as $c_p \mathrm{d}T/\mathrm{d}t = j^2\eta$, with c_p being the specific heat of solid copper, generally a function of temperature. By integrating this relation, we obtain the "fuse" action integral

$$\int_{T_0}^{T_1} \frac{c_p}{\eta}\mathrm{d}T = \int_0^{t_p} j^2\,\mathrm{d}t\,, \tag{9}$$

which relates the material properties to the time integral of the current density. At some value of this integral, the coils will melt and the current will be interrupted. Since j is set by the peak field requirement to minimize the action integral, we need to reduce the time of current propagation t_p. Whether this time will be sufficient for the current to reach its peak value is determined by comparing t_p to the time constant $\tau = L/R$ of the discharge. Expressing the joule heating energy deposited from $t = 0$ to t_p, in terms of the peak current $I_{\max}$ and the average resistance $\overline{R}(B,T)$, and using the time constant τ, we obtain the ratio of the maximum magnetic energy $E_m(t_p)$ to the heating in the coils, as the ratio of the pulse rise time t_p to the circuit time constant,

$$E_j(t_p) = \int_0^{t_p} R(t) I^2 \mathrm{d}t \approx \overline{R}(B,T)\frac{I_{\max}^2}{2} t_p$$

$$\approx \frac{t_p}{2\tau} L I_{\max}^2 = \frac{t_p}{\tau} E_m(t_p). \quad (10)$$

This ratio needs to be minimized for the most-efficient energy transfer. Based on these considerations, we have chosen a capacitor bank consisting of two 100-nF capacitors connected in parallel, with total inductance of ~8 nH. These are S-series[15] plastic case capacitors (Fig. 110.5) from General Atomics, rated for 40 kV, and pulsed currents of 50 kA. Their combined ESR value for the fundamental frequency of the discharge is less than 2.5 mΩ. Charged to their rated voltage, the capacitors can store 160 J but have been used routinely at 30-kV charge voltage, storing 90 J of energy. The same restrictions (as-low-as-possible inductance and resistance) apply to the discharge switch and transmission wiring. In the design, a very-low-inductance, coaxial, laser-triggered spark gap is mounted directly to the capacitors, while the return path consists of two 3-in.-wide copper bars (Fig. 110.5). This compact package can fit in a small vessel that can be placed in an OMEGA TIM (ten-inch manipulator) along with its dedicated charging circuitry. This way, the transmission length is greatly reduced in favor of the desired small overall inductance, and no high-voltage lines are fed into the target chamber.

A CAD drawing of the MIFEDS device as placed in the TIM rolling platform is shown in Fig. 110.6. There are two distinct compartments: In the front is the energy storage and switch block, while the charger and protection circuitry are located in the back. There is a metal barrier between the compartments, with openings only for the trigger beam and the charging cables. This way, the capacitive coupling of noise from the rapid, high-current discharge in the front into the components in the back is reduced. Those components consist of (a) the power supply—a 30-W dc-to-dc converter[16] with a supply voltage of 24-V dc and a rated peak voltage of 40 kV

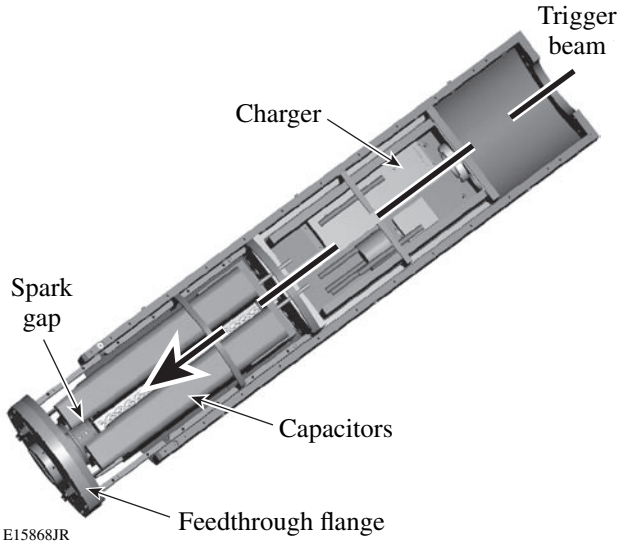

Figure 110.6
CAD drawing of the main MIFEDS components inside the air box that is mounted to the TIM rolling platform.

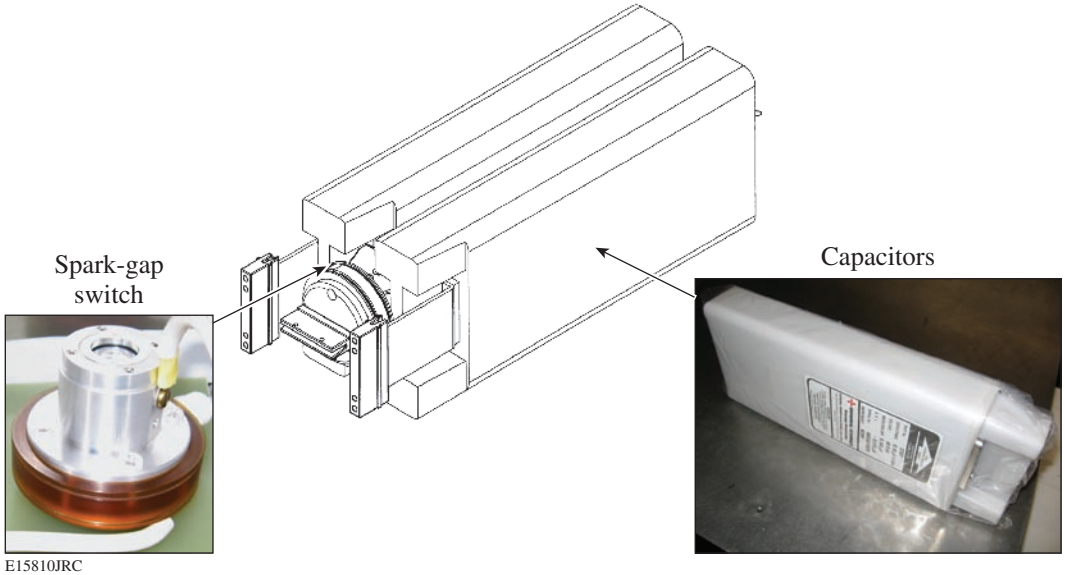

Figure 110.5
Low-inductance assembly of the energy storage capacitors and the laser-triggered spark-gap switch. The actual devices are also shown.

at maximum current of 750 μA; (b) a high-voltage relay, used to dump to ground the residual energy immediately after discharge; and (c) an array of diodes and current-limiting resistors to protect the high-voltage power supply from reverse voltage transients, a pressure sensor, a low-voltage solid-state relay, and an interface board to monitor and control the charge cycle. Careful packaging was necessary to be able to place and safely operate these components at >30 kV. Care was taken to provide a clear optical path for the trigger laser beam along the axis of the air box.

Magnetic-Field Measurements

The main diagnostic method for the seed magnetic field during the development of MIFEDS has been magneto-optical. Faraday rotation (Fig. 110.7) was used to measure the fields generated between the MIFEDS coils when testing coil geometry, transmission line design, and the high-voltage switch. The probe laser was a temperature-stabilized, frequency-doubled, cw Nd-YAG laser providing 50 mW of power at 532-nm wavelength. The probe, placed between the two coils, was a 1-mm-thick, terbium-doped glass disk with a 1.5-mm diameter and Verdet constant $V = 100\ \mathrm{rad}T^{-1}\mathrm{m}^{-1}$. Because of the strong fields expected, the two polarizers were coaligned for maximum transmission of the linearly polarized laser light; this is not the highest sensitivity configuration but the easiest to work with, especially when rotation angles larger than 90° are possible. The drop in the signal due to Faraday rotation in the glass sample during the magnetic pulse was then observed and the field determined from the detected light intensity $I_{\mathrm{det}}(t)$, $I_{\mathrm{det}}(t) = I_0 \cos^2\left[\theta_{\mathrm{rot}}(t)\right]$, where $\theta_{\mathrm{rot}}(t) = V\overline{B}_z(t)d_z$ is the Faraday rotation angle as a function of the average axial field in the sample and its thickness d_z. Figure 110.8 shows the change in laser intensity triggered by the Faraday rotation and recorded by a fast optical detector connected to an oscilloscope. Three intensity traces show very repetitive magnetic pulses with an average pulsewidth of ~400-ns FWHM and decay time of the order of 1.5 μs. The maximum magnetic field at the center of the coil ranges from 14 to 15.7±0.3 T (10 T = 0.1 MG). These fields correspond to a total coil current of 79.3 kA for a separation D = 2.4 mm and a coil radius of 2 mm used in these tests. The magnetostatic Radia simulations,[14] which account for the aspect ratio of the coil, gave a total current of 76 kA for the same peak field.

A simple analytical model was developed to look at the temporal behavior of the coil current. It is based on the equivalent, damped LRC circuit, where the reference damping α was given by an average value of the time-dependent coil resistance. The current from the model,

$$I_{\mathrm{mod}}(t) = \frac{\omega_0^2 + \alpha^2}{\sqrt{\omega_0^2 - \alpha^2}} CV_{\mathrm{max}} \exp(-\alpha t) \sin\left(\sqrt{\omega_0^2 - \alpha^2}\, t\right), \quad (11)$$

where V_{max} is the charging voltage, C is the capacitance, and ω_0 is the fundamental frequency of the circuit, was then converted to the equivalent Faraday rotation signal, using Eq. (8). The best-fit parameters were sought and the fit is shown in Fig. 110.9. The best-fit parameters are $R_{\mathrm{avg}} = 0.21\ \Omega$, $\omega_0 = 8.78 \times 10^6$ rad/s, and $\alpha = 2.1 \times 10^6$ rad/s. From the fit we then determined a total circuit inductance of 65 nH, which is in line with calculations for the individual components. The agreement between the

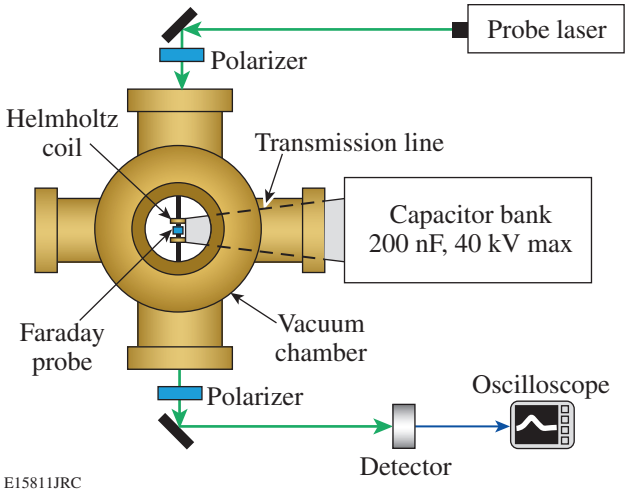

Figure 110.7
Faraday rotation setup for the measurement of the seed magnetic fields on the benchtop.

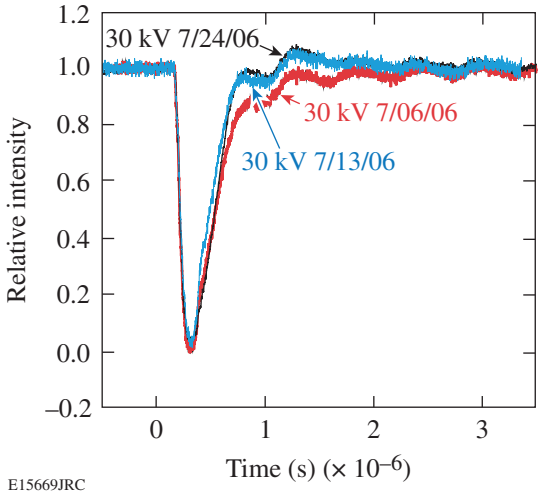

Figure 110.8
Faraday rotation data over two weeks of MIFEDS discharges. The data show good repeatability with a pulse duration of ~400-ns FWHM and a rise time of ~160 ns.

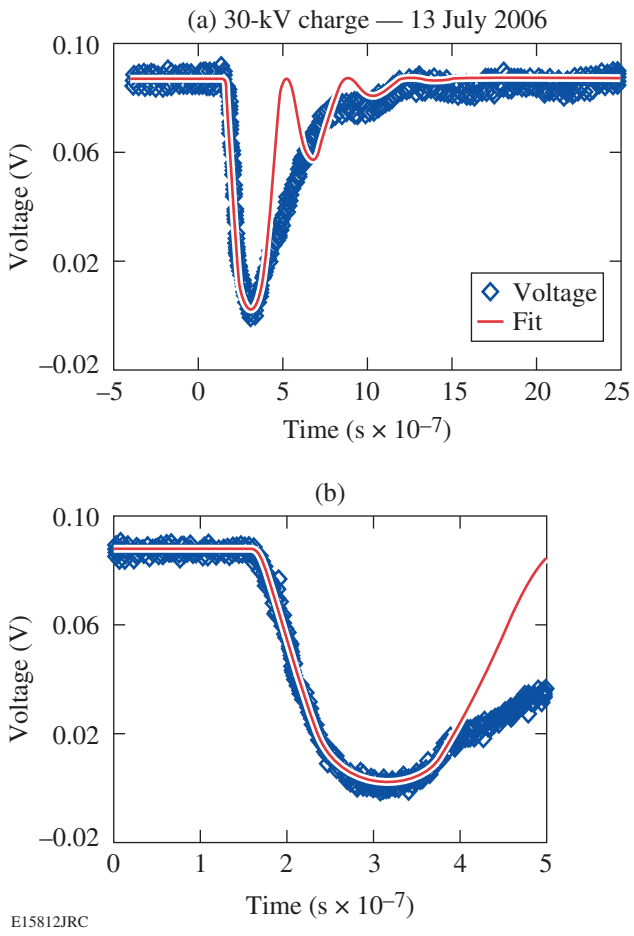

Figure 110.9
A simple analytical model was fit to the data. It matches the experiment very well until after the current peak.

experiment and the analytical model is very good until after the peak of the current pulse. At later times, the experimental data show rapid change in the time-dependent resistance of the circuit, which becomes overdamped. Several possible reasons for that include joule heating in the coil, extinguishing of the streamer in the spark-gap switch, or even change in the contact resistance somewhere in the transmission path. From a design standpoint this is beneficial since we are able to reach the peak current while the load is less resistive. The detrimental voltage reversal, characteristic of underdamped circuits, is avoided with this rapid increase of the circuit resistance.

Initial Experiments on OMEGA

Before testing it on OMEGA, the MIFEDS device was qualified in the diagnostic TIM facility, where a number of discharges were performed to monitor the charge cycle, EMI noise, gas pressure stability, and other parameters. The interfacing of MIFEDS to the diagnostic TIM closely emulated the OMEGA chamber/TIM setup (shown in Fig. 110.10). An optical Faraday rotation setup was arranged and the magnetic field pulses were recorded. The precise time delay from the triggering of a discharge to the time of peak magnetic field was established. The delay was highly repetitive at 310 ns with standard deviation of about 18 ns. One of the concerns was the survival of the cylindrical target during the rise time of the magnetic pulse. The possibility of destroying the target before the laser shot endangers the OMEGA laser components since some of the unterminated beams can back-propagate at full energy. A special safety circuit was implemented to prevent the propagation of OMEGA beams in the case of MIFEDS prefire (Fig. 110.10). It is connected to a pickup coil placed at the spark-gap switch in MIFEDS to detect the current pulse.

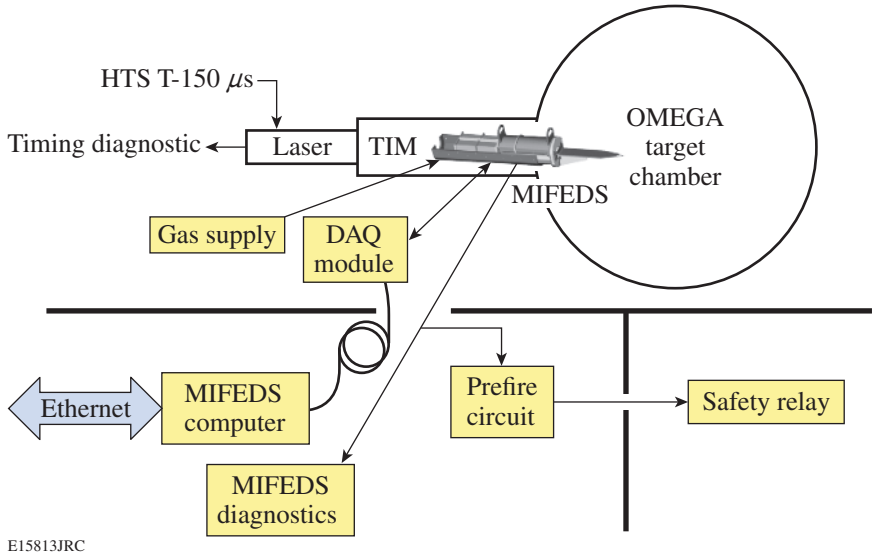

Figure 110.10
Setup of the MIFEDS infrastructure in the OMEGA Target Bay. The three main components are the switching, control and monitoring, and safety circuits.

It was established that the target needs a 100-nm Al overcoat to provide reasonable retention of the gas at 3- to 5-atm pressure. This raised an important question about the time needed by the seed field to diffuse through the aluminum before an OMEGA shot. If the field is excluded from the inside of the target, the consequent flux compression would be impeded. For this purpose we designed a special experiment in the diagnostic TIM facility, using the Faraday rotation setup. An aluminized CH shell with all of the target parameters except for size (its diameter was 1.5 mm to accommodate a Faraday rotator glass sample) was placed between the MIFEDS coils, and several discharges were performed. The difference in the magnetic pulse rise time of these discharges and the earlier experiments with the stand-alone Faraday probe was within a typical time jitter of 16 ns. From this, it was concluded that the Al layer, much thinner than the skin depth of 60 μm at the fundamental frequency of the pulse, was not a barrier for the seed field.

Initial experiments were conducted to integrate MIFEDS into OMEGA and test the experimental geometry, to develop the proton backlighter diagnostic, and to measure the convergence ratio of cylindrical implosions. Forty OMEGA beams were radially incident on the cylindrical target, while the remaining 20 were used to generate 14.7-MeV probe protons in a separate D^3He-filled glass shell for magnetic-field measurement. The technique is a further development of the one described in Ref. 17. Figure 110.11(a) shows a typical configuration with a cylindrical target mounted between the MIFEDS coils and imaged with the OMEGA Target Viewing System. One can also see the outlines of rectangular and circular polyimide plugs used in this case, as well as the crossbeam on the target stalk used to correctly orient the axis of the cylinder. The inset shows a time-integrated, x-ray self-emission image of the imploded target. The enhanced emission of x rays with average energy in the 1-keV range is seen from the hot compressed core. The 450-μm-diam glass microballoon used as the proton backlighter is visible in the lower right corner. From these experiments, the time of peak compression was established to within 100 ps. In comparison, the duration of the proton burst is ~150 ps (Ref. 17). The detector medium for the protons is a two-layer package of 1-mm-thick, CR-39 plastic track detectors, shielded by Al filters. The initially chosen filter thickness was not optimal, as can be seen from Fig. 110.11(b) where the proton density map at the surface of the second CR-39 detector is shown. The darker areas have a higher proton density. One can see the deficiency of protons in the area of the compressed core, which is undesirable since these are the particles to be deflected by the compressed fields. Monte Carlo simulations based on the experimental data are ongoing to identify the optimal filter thickness for the next experiment. The goal is to match to the CR-39 detector surface a specific portion of the energy loss versus depth curve (near but before the Bragg peak) of the particles that traverse the compressed core, so that these specific particles are centered in the limited readout energy band with a maximum signal-to-noise ratio. Upcoming experiments will utilize the improved detector geometry.

Conclusions

The concept of laser-driven magnetic-flux compression was briefly introduced with emphasis on its application to the

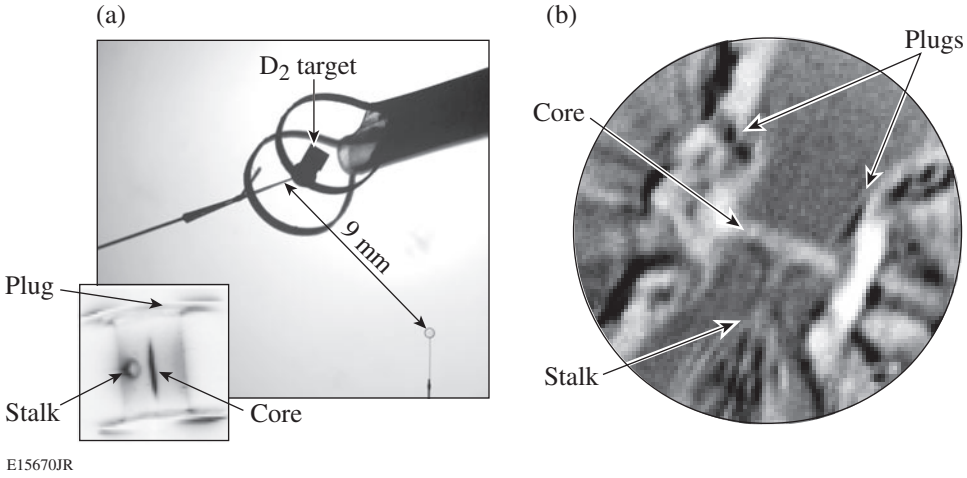

Figure 110.11
(a) D_2-filled shell placed between the MIFEDS coils and imaged with the OMEGA Target Viewing System. The proton backlighter is visible in the lower right. The inset depicts a time-integrated x-ray self-emission image showing the enhanced emission from the compressed hot core. (b) Density map of protons imaging the target near peak compression. The protons passing through the core are slowed down below the detection threshold.

improvement of direct-drive laser fusion. The confinement and amplification of seeded magnetic flux in cylindrical, D_2-filled plastic shells, irradiated by the OMEGA laser, were discussed in this context. A gigawatt seed-field generator that can discharge 100 J of energy in 400 ns was designed and built in a compact package for these experiments. Its spatial and temporal parameters were optimized for the delivery of a strong magnetic pulse in the small (a few tens of mm^3) laser–target interaction volume of OMEGA. Seed magnetic fields larger than 0.15 MG were measured in the center of the low-mass double-coil assembly. A proton deflectrometry technique is being developed for the observation of the flux compression in an optically thick cylindrical target. The initial proton backlighting experiments helped establish the relative timing of the proton pulse with respect to the time of peak convergence of the target. The data aided the matching of the CR-39 detector surface with the appropriate portion of the dose versus depth curve (near but before the Bragg peak) for the protons that are slowed down through the core. These form the basis for future flux-compression experiments, first in cylindrical and later in spherical geometry. Applications of the laser-driven flux compression will not be limited to ICF studies. Work is in progress to use the seed field for OMEGA experiments in the context of laboratory astrophysics experiments, such as magnetized plasma jets. In addition, a scheme that uses moderate flux compression in cylindrical geometry is being evaluated for the confinement of electron–positron plasma[18] generated in an integrated OMEGA/OMEGA EP[19] experiment.

ACKNOWLEDGMENT

One of the authors (O. V. Gotchev) would like to thank Dr. A. V. Okishev, W. A. Bittle, G. Brent, and G. Raffaele-Addamo for their expert advice and helpful discussions. This work was supported by the U.S. Department of Energy Office of Fusion Energy Sciences under Grants DE-FG02-04ER54768 and DE-FC02-ER54789 and by the Office of Inertial Confinement Fusion under Cooperative Agreement No. DE-FC52-92SF19460, as well as the University of Rochester and the New York State Energy Research and Development Authority. The support of DOE does not constitute an endorsement by DOE of the views expressed in this article.

REFERENCES

1. S. E. Bodner, D. G. Colombant, J. H. Gardner, R. H. Lehmberg, S. P. Obenschain, L. Phillips, A. J. Schmitt, J. D. Sethian, R. L. McCrory, W. Seka, C. P. Verdon, J. P. Knauer, B. B. Afeyan, and H. T. Powell, Phys. Plasmas **5**, 1901 (1998).

2. R. L. McCrory, D. D. Meyerhofer, S. J. Loucks, S. Skupsky, R. Betti, T. R. Boehly, T. J. B. Collins, R. S. Craxton, J. A. Delettrez, D. H. Edgell, R. Epstein, K. A. Fletcher, C. Freeman, J. A. Frenje, V. Yu. Glebov, V. N. Goncharov, D. R. Harding, I. V. Igumenshchev, R. L. Keck, J. D. Kilkenny, J. P. Knauer, C. K. Li, J. Marciante, J. A. Marozas, F. J. Marshall, A. V. Maximov, P. W. McKenty, S. F. B. Morse, J. Myatt, S. Padalino, R. D. Petrasso, P. B. Radha, S. P. Regan, T. C. Sangster, F. H. Séguin, W. Seka, V. A. Smalyuk, J. M. Soures, C. Stoeckl, B. Yaakobi, and J. D. Zuegel, J. Phys. IV France **133**, 59 (2006).

3. R. Betti, K. Anderson, T. R. Boehly, T. J. B. Collins, R. S. Craxton, J. A. Delettrez, D. H. Edgell, R. Epstein, V. Yu. Glebov, V. N. Goncharov, D. R. Harding, R. L. Keck, J. H. Kelly, J. P. Knauer, S. J. Loucks, J. A. Marozas, F. J. Marshall, A. V. Maximov, D. N. Maywar, R. L. McCrory, P. W. McKenty, D. D. Meyerhofer, J. Myatt, P. B. Radha, S. P. Regan, C. Ren, T. C. Sangster, W. Seka, S. Skupsky, A. A. Solodov, V. A. Smalyuk, J. M. Soures, C. Stoeckl, W. Theobald, B. Yaakobi, C. Zhou, J. D. Zuegel, J. A. Frenje, C. K. Li, R. D. Petrasso, and F. H. Séguin, Plasma Phys. Control. Fusion **48**, B153 (2006).

4. R. Betti and C. Zhou, Phys. Plasmas **12**, 110702 (2005).

5. P. W. McKenty, V. N. Goncharov, R. P. J. Town, S. Skupsky, R. Betti, and R. L. McCrory, Phys. Plasmas **8**, 2315 (2001).

6. C. M. Fowler, W. B. Garn, and R. S. Caird, J. Appl. Phys. **31**, 588 (1960).

7. A. D. Sakharov *et al.*, Sov. Phys. Doklady AN SSSR **165**, 65 (1965).

8. A. I. Bykov *et al.*, Physica B **294–295**, 574 (2001).

9. T. R. Boehly, D. L. Brown, R. S. Craxton, R. L. Keck, J. P. Knauer, J. H. Kelly, T. J. Kessler, S. A. Kumpan, S. J. Loucks, S. A. Letzring, F. J. Marshall, R. L. McCrory, S. F. B. Morse, W. Seka, J. M. Soures, and C. P. Verdon, Opt. Commun. **133**, 495 (1997).

10. M. A. Liberman and A. L. Velikovich, J. Plasma Phys. **31**, 369 (1984).

11. A. L. Velikovich *et al.*, Sov. Phys.-JETP **61**, 261 (1985).

12. F. Herlach, Rep. Prog. Phys. **62**, 859 (1999).

13. N. W. Jang, R. Betti, J. P. Knauer, O. Gotchev, and D. D. Meyerhofer, Bull. Am. Phys. Soc. **51**, 144 (2006).

14. O. Chubar, P. Elleaume, and J. Chavanne, J. Synchrotron Radiat. **5**, 481 (1998).

15. Series S/SS High Voltage Rep-Rate Capacitors, General Atomics Energy Products, General Atomics Electronic Systems, Inc., San Diego, CA 92123, http://www.gaep.com/series-s-ss-capacitors.html (18 June 2007).

16. 40A Series, part no. 40A24N30, Ultravolt, Inc., Ronkonkoma, NY 11779, http://www.ultravolt.com/coa-40aser.htm (18 June 2007).

17. C. K. Li, F. H. Séguin, J. A. Frenje, J. R. Rygg, R. D. Petrasso, R. P. J. Town, P. A. Amendt, S. P. Hatchett, O. L. Landen, A. J. Mackinnon, P. K. Patel, V. Smalyuk, J. P. Knauer, T. C. Sangster, and C. Stoeckl, Rev. Sci. Instrum. **77**, 10E725 (2006).

18. J. Myatt, A. V. Maximov, and R. W. Short, Bull. Am. Phys. Soc. **51**, 25 (2006).

19. L. J. Waxer, D. N. Maywar, J. H. Kelly, T. J. Kessler, B. E. Kruschwitz, S. J. Loucks, R. L. McCrory, D. D. Meyerhofer, S. F. B. Morse, C. Stoeckl, and J. D. Zuegel, Opt. Photonics News **16**, 30 (2005).